Frequency Domain Modelling and Stability Analysis of a DFIG-based Wind Energy Conversion System Under None-compensated AC Grids: Impedance Modelling Effects and Consequences on Stability

Chen Zhang [1], Xu Cai[1], Marta Molinas [2], Atle Rygg[2]

[1] Department of Electrical Engineering, Shanghai Jiao Tong University, Shanghai, People's Republic of China
[2] Department of Engineering Cybernetics, Norwegian University of Science and Technology, Trondheim, Norway
*xucai@sjtu.edu.cn

Abstract: Impedance-based frequency domain method is an effective tool for the stability assessment of a doubly-fed induction generator (DFIG) system. Several impedance models have been proposed recently, however, these models are usually associated with model reductions since the complexity in achieving a detailed DFIG model. This may lead to unreliable stability results under certain conditions, and a clarification of this modeling effects is lacking in the literature. Therefore, this paper aims to address this issue by developing a detailed DFIG impedance model. To achieve this target, a modular modeling technique is proposed instead of the conventional linearization by parts, for which the components of a DFIG system are modeled as multi-port modules. Through this method, the detailed DFIG model together with four types of reduced-order models can be derived efficiently. The detailed DFIG model is verified by the measured frequency responses in PSCAD/EMTDC, along with its correctness in Nyquist-based stability analysis. Subsequently, four types of the reduced-order models are compared with the detailed one in terms of Nyquist plots, so that their performance and effectiveness for stability analysis are clarified. Besides, conclusions regarding the reduced-order models are also verified by time domain simulations.

1. Introduction

Voltage source converters (VSCs) are widely adopted for the grid integration of renewable energies, such as wind and solar [1]. However, grid-integration of these VSC-based renewable power generations can be challenging, not only because of their intrinsic fluctuation [2], but also the new dynamics brought about by the VSCs [3].

Previous experience has revealed that the wind farms are inclined to oscillate when connecting to a *compensated* AC grid. An early report about this was presented in [4], where the doubly-fed induction generator (DFIG) based wind farms in Texas (USA) were suffered from the so-called sub-synchronous resonance (SSR). Since then, extensive works have been done with respect to this, and the mechanisms behind this resonance are well-established now, which can be the torsional interaction (TI) [5], the induction generator effect (IGE) [6], and the sub-synchronous interaction (SSI). In particular, the SSI issue is analyzed in detail since it is related to the converter controls and are relatively new for the conventional power system. Specifically, for the DFIG wind turbines, it now becomes widely accepted that the rotor side converter (RSC) has more evident effects than the grid side converter (GSC) with respect to the SSR. Hence, the GSC is usually omitted for modelling if this type of SSR is aimed at [6]. Besides, many SSR-mitigation methods have also been proposed by either modifying the original controls [8] or utilizing ancillary devices [9].

During this period of analysis, the electromechanical dynamics of rotating machines (e.g. the synchronous generator) still dominate the system's behavior, thus dynamics specific to power electronic devices are not evident. Until recently, due to the fast growth of renewable energies, VSCs become ubiquitous in power systems, invoking new dynamical issues. For example, a new type of SSR was reported in China recently [10], which is quite different from the DFIG-SSR. In this case, the oscillation occurred between a full-scale-converter based wind farm and a *non-compensated* AC grid. This issue gains immediate attention and a preliminary mechanism about this can be understood as that (e.g. [3] and [10]), the VSC introduces capacitive effect to the inductive AC grid, forming an equivalent RLC circuit. Therefore, oscillation may occur if the net damping of the circuit is negative, and this negative damping can be a consequence of the phase-locked-loop (PLL) [3]. Besides, a recent work in [11] also points out that the outer control loops of the VSC can also cause instability.

In general, these emerging issues motive the needs for a thorough stability analysis as well as providing useful methods for the VSC-based systems. Among them, the impedance-based frequency domain analysis method is prevailing since the impedance can be obtained either by analytical modelling or measurements [12]. Moreover, the well-known Nyquist criterion can be applied for stability assessment [13], which is efficient and more acceptable for electrical engineers.

Impedance modelling of a VSC can be fulfilled through different methods, e.g. the harmonic linearization method [12] for the sequence impedance modelling [14], and the typical *dq* domain linearization method for the *dq* impedance modelling [15]. Recent works e.g. a phasor-based [16], a modified sequence domain based [17], and a complex transfer-function based (e.g. [18] and [19]) method, also provide some new perspectives. From which, the VSC properties can be interpreted better, e.g. the mirror frequency coupling effect [17] or the sequence coupling effect [20].

Definitely, these techniques are applicable for the impedance modelling of a DFIG wind system. However, it can be challenging since the typology of a DFIG is much more complicated than a single VSC. Particularly, its GSC and RSC are coupled both on the dc and ac side. Therefore, impedance modelling of a DFIG system usually associated with model reductions. For example, recent works e.g. [21] and [22] developed a DFIG impedance model with a constant dc-link voltage assumption, whereby the GSC and RSC can be modelled separately. However, the effects of these model

1

assumptions on stability have not been properly addressed and evaluated.

Therefore, this work aims to address this issue by providing a detailed DFIG impedance model, and by clarifying the associated model reduction effects on stability analysis, particularly, the stability conclusion. This paper is organized as follows:

In section 2, the modular modelling method is introduced and applied to derive the detailed DFIG impedance model. Section 3 performs a thorough verification of the detailed DFIG model. Next, four types of reduced-order models are developed by means of the modular modelling approach, in section 4, and their performance and effectiveness on stability analysis are discussed and clarified. Finally, section 5 draws the main conclusions.

2. Modular impedance modeling of the DFIG system

2.1. System description

Fig. 1 presents a typical DFIG-based wind system. The electrical parts are shown in detail, whereas the mechanical parts (e.g. wind rotor and drive chain etc.) are neglected since this work is focused on the converter control-related stability issues.
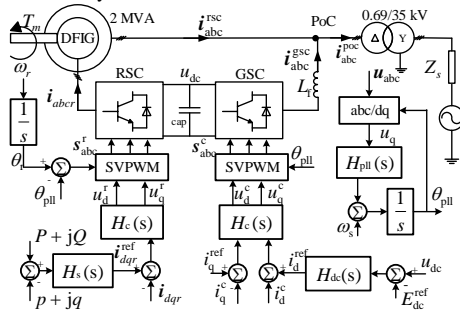

Fig. 1 Schematic of a DFIG-based wind power system

Generally, GSC controls the dc voltage, whereas the RSC fulfills the maximum power point tracking (MPPT) (see [23] for details). Both of the GSC and RSC have identical inner current control loops. The step-up transformer is considered since it can introduce a relatively large leakage inductance to the line impedance. The grid is represented by a Thevenin equivalent voltage source. The total grid impedance seen from point of connection (POC) can be quantified by the short circuit ratio (SCR). It is noted that since all the controls are in the *dq* frame, which relies on the proper functioning of a PLL.

2.2. Modular modeling method

Impedance modelling of a single VSC is intuitive since it only contains two ac ports in *dq* domain (e.g. u_d and u_q). However, for a DFIG system, the GSC and RSC are interconnected not only at the dc side but also the ac side (via the stator of DFIG), resulting in a coupled ac/dc system. Therefore, directly modelling from the ac side with a step-by-step linearization method is inefficient and even unfeasible in some cases.

To overcome this issue, this work adopts a modular modelling method. As illustrated in Fig. 2, the GSC and RSC

can be modeled as *three-port* modules, where the *d* and *q* axis of the ac voltage can be the two ports, and the third port is the dc voltage of the converter. Accordingly, the *dq* and dc currents can be chosen as the three-port outputs. Note that the DFIG winding circuit is included in the RSC module.
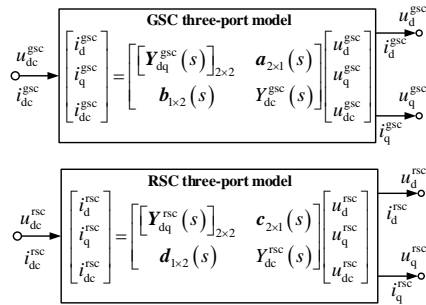

Fig. 2 Modular representation of the RSC and GSC

The major benefit of this method is that, once the GSC and the RSC module are established, they can be manipulated via Kirchoff's current and voltage law to derive the detailed DFIG model, as well as the reduced-order efficiently.

2.3. Derivation of the GSC and RSC module

In this subsection, the analytical modelling of the GSC and RSC module will be presented. Generally, they can be derived from the *dq* impedance modelling technique as presented in [15].

Previously, authors of this work have proposed a *modified* sequence domain modelling method [17]. In essence, it is a linear transformed *dq* impedance but inheriting the major properties of the sequence impedance. To the authors' experience, the modified sequence impedance exhibits better numerical performance, which is more suitable for a complex system analysis (e.g. high order). Therefore, the DFIG will be modelled in the modified sequence domain.

2.3.1 Modelling the GSC module: Derivation of the GSC model in the modified sequence domain can be fulfilled by the following two steps: 1) the first step is to linearize the control blocks of GSC (Fig. 1) in *dq* domain [15]; 2) the second step is to convert them into the modified sequence domain, this can be found in a previous study [24]. This work will not look into such details to maintain a compact structure.

Generally, the GSC dynamics can be represented by a set of linearized equations in the *dq* frame as follows (see appendix 8.1 for details):

$$\begin{cases} H_c(s)\left(\boldsymbol{i}_{dq}^{ref} - \boldsymbol{i}_{dq}^{gsc} + \mathrm{j}\boldsymbol{I}_{c0}\Delta\theta_{pll}\right) = \boldsymbol{d}_{dq}^{gsc} - \mathrm{j}\boldsymbol{D}_{c0}\Delta\theta_{pll} \\[2mm] \Delta\theta_{pll} = \dfrac{U_0 H_{pll}(s)}{1+U_0 H_{pll}(s)}\dfrac{u_q}{U_0} = T_{pll}(s)\dfrac{u_q}{U_0} \\[2mm] i_d^{ref} = H_{dc}(s)u_{dc}, i_q^{ref} = 0 \\[2mm] \boldsymbol{u}_{dq}^{gsc} = \boldsymbol{D}_{c0}u_{dc} + V_{dc0}\boldsymbol{d}_{dq}^{gsc} = Z_f(s)\boldsymbol{i}_{dq}^{gsc} + \boldsymbol{u}_{dq}^{poc} \\[2mm] i_{dc}^{gsc} = 1.5\,\mathrm{Re}\left\{\boldsymbol{D}_{c0}\left(\boldsymbol{i}_{dq}^{gsc}\right)^* + \boldsymbol{I}_{c0}^*\boldsymbol{d}_{dq}^{gsc}\right\} \end{cases} \quad (1)$$

2

Decomposing the vectors (e.g. $\mathbf{i}_{dq}$) in dq frame yields:

$$\mathbf{i}_{dq} = \mathbf{i}_p e^{j\omega} + \left(\mathbf{i}_n e^{j\omega}\right)^*, \quad \forall \omega$$

, where $\mathbf{i}_p$ and $\mathbf{i}_n$ are the positive- and negative-sequence components. Further, the following relationship is established:

$$\begin{bmatrix} \mathbf{i}_p \\ \mathbf{i}_n \end{bmatrix} = \frac{1}{2} \begin{bmatrix} 1 & j \\ 1 & -j \end{bmatrix} \begin{bmatrix} \mathbf{i}_d \\ \mathbf{i}_q \end{bmatrix} \quad (2)$$

this is basically the method for transforming impedance in dq domain to modified sequence domain as discussed in [17] and [24].

Given by this method, (1) can be transformed into modified sequence domain, yields the GSC module (i_p^{gsc}, i_n^{gsc} are positive if flowing into the grid, i_{dc}^{gsc} is positive if flowing into GSC) as:

$$\begin{bmatrix} i_p^{gsc} \\ i_n^{gsc} \end{bmatrix} = \mathbf{Y}_{pn}^{gsc} \begin{bmatrix} u_p^{poc} \\ u_n^{poc} \end{bmatrix} + \mathbf{a}_{2\times1} u_{dc}^{gsc} \quad (3)$$

and,

$$i_{dc}^{gsc} = \mathbf{b}_{1\times2} \begin{bmatrix} u_p^{poc} \\ u_n^{poc} \end{bmatrix} + Y_{dc}^{gsc} u_{dc}^{gsc} \quad (4)$$

Please see the appendix for $\mathbf{Y}_{pn}^{gsc}, \mathbf{a}_{2\times1}, \mathbf{b}_{1\times2}$ and Y_{dc}^{gsc} models.

2.3.2 Modelling the RSC module: The RSC module can be derived in a similar way as the GSC module. Generally, the RSC can be represented by a set of linearized equations in dq frame as (see the appendix 8.2 for details):

$$\begin{cases} H_c(s)\left(\mathbf{i}_{dq}^{ref} - \mathbf{i}_{dq}^r + j\mathbf{I}_{r0}\Delta\theta_{pll}\right) = \mathbf{d}_{dq}^r - j\mathbf{D}_{r0}\Delta\theta_{pll} \\ \left(\mathbf{i}_{dq}^{ref}\right)^* = -H_s(s)(p+jq) \\ \mathbf{u}_{dq}^r = \mathbf{D}_{r0}u_{dc}^{rsc} + V_{dc0}\mathbf{d}_{dq}^r \\ \mathbf{u}_{dq}^r = R_r\mathbf{i}_{dq}^r + (s+js_0\omega_s)\left(L_r\mathbf{i}_{dq}^r - L_m\mathbf{i}_{dq}^{rsc}\right) \\ \mathbf{u}_{dq}^{poc} = -R_s\mathbf{i}_{dq}^{rsc} + (s+js_0\omega_s)\left(L_m\mathbf{i}_{dq}^r - L_s\mathbf{i}_{dq}^{rsc}\right) \\ i_{dc}^{rsc} = 1.5\,\mathrm{Re}\left\{\mathbf{D}_{r0}\left(\mathbf{i}_{dq}^r\right)^* + \mathbf{I}_{r0}^*\mathbf{d}_{dq}^r\right\} \\ p = 1.5\,\mathrm{Re}\left\{\mathbf{U}_0^{poc}\left(\mathbf{i}_{dq}^{rsc}\right)^* + \mathbf{I}_{s0}^*\mathbf{u}_{dq}^{poc}\right\} \\ q = 1.5\,\mathrm{Im}\left\{\mathbf{U}_0^{poc}\left(\mathbf{i}_{dq}^{rsc}\right)^* + \mathbf{I}_{s0}^*\mathbf{u}_{dq}^{poc}\right\} \end{cases} \quad (5)$$

Then, transforming (5) into the modified sequence domain by the same method, yields (dc current i_{dc}^{rsc} is positive if flowing into RSC, and ac currents $\mathbf{i}_{dq}^r$ and $\mathbf{i}_{dq}^{rsc}$ are positive if flowing into the grid):

$$\begin{bmatrix} i_p^{rsc} \\ i_n^{rsc} \end{bmatrix} = \mathbf{Y}_{pn}^{rsc} \begin{bmatrix} u_p^{poc} \\ u_n^{poc} \end{bmatrix} + \mathbf{c}_{2\times1} u_{dc}^{rsc} \quad (6)$$

and,

$$i_{dc}^{rsc} = \mathbf{d}_{1\times2} \begin{bmatrix} u_p^{poc} \\ u_n^{poc} \end{bmatrix} + Y_{dc}^{rsc} u_{dc}^{rsc} \quad (7)$$

Please see the appendix for $\mathbf{Y}_{pn}^{rsc}, \mathbf{c}_{2\times1}, \mathbf{d}_{1\times2}$ and Y_{dc}^{rsc} models.

Finally, both the GSC and RSC module are obtained. In which, the GSC module is comprised of (3) and (4),

whereas the RSC module is comprised of (6) and (7). Note that in Fig. 2, the subscripts "dq" should be replaced with "pn".

2.4. Derivation of the detailed DFIG admittance model

The ac side DFIG impedance model (i.e. seen from the POC) can be derived by eliminating the dc ports from the RSC and GSC modules using the following equation:

$$\begin{cases} i_{dc}^{rsc} + i_{dc}^{gsc} = -s \cdot C_{cap} u_{dc} \\ u_{dc}^{rsc} = u_{dc}^{gsc} = u_{dc} \end{cases} \quad (8)$$

Substituting it into the summation of (4) and (7) gives:

$$u_{dc}^{rsc} = -\frac{\left(\mathbf{d}_{1\times2} + \mathbf{b}_{1\times2}\right)}{Y_{dc}^{all}} \begin{bmatrix} u_p^{poc} \\ u_n^{poc} \end{bmatrix} \quad (9)$$

where $Y_{dc}^{all} = Y_{dc}^{rsc} + Y_{dc}^{gsc} + s \cdot C_{cap}$.

Then, substituting it into the summation of (3) to (6), yields:

$$-\begin{bmatrix} i_p^{poc} \\ i_n^{poc} \end{bmatrix} = \mathbf{Y}_{pn}^{DFIG} \begin{bmatrix} u_p^{poc} \\ u_n^{poc} \end{bmatrix}$$

$$\mathbf{Y}_{pn}^{DFIG} = -\mathbf{Y}_{pn}^{gsc} - \mathbf{Y}_{pn}^{rsc} + \frac{\left(\mathbf{a}_{2\times1} + \mathbf{c}_{2\times1}\right)\left(\mathbf{d}_{1\times2} + \mathbf{b}_{1\times2}\right)}{Y_{dc}^{all}} \quad (10)$$

Finally, the detailed DFIG admittance model is obtained, i.e. $\mathbf{Y}_{pn}^{DFIG}$. In which, it can be clearly observed that $-\mathbf{Y}_{pn}^{gsc}, -\mathbf{Y}_{pn}^{rsc}$ are the ac side admittances of RSC and GSC under a constant dc voltage assumption [22]. Hence, the additional term: $\left(\mathbf{a}_{2\times1} + \mathbf{c}_{2\times1}\right)\left(\mathbf{d}_{1\times2} + \mathbf{b}_{1\times2}\right)/Y_{dc}^{all}$ can be interpreted as the dc-coupling of the RSC and GSC.

3. Validation of the detailed DFIG impedance model

In this section, the detailed DFIG model (10) will be verified through the measured frequency responses along with the Nyquist-based analysis.

3.1. Method for measuring modified sequence impedance from simulations

The DFIG system as shown in Fig. 1 is built in PSCAD/EMTDC. The multi-run module is utilized to inject one single-tone perturbation of each run, and the frequency is swept from 2 Hz to 100 Hz with an increment of 2 Hz.
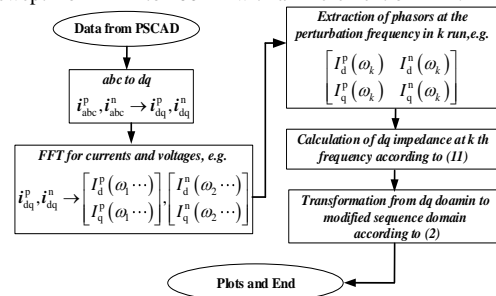
Fig. 3 *A flowchart of measuring the modified sequence impedance from simulations*
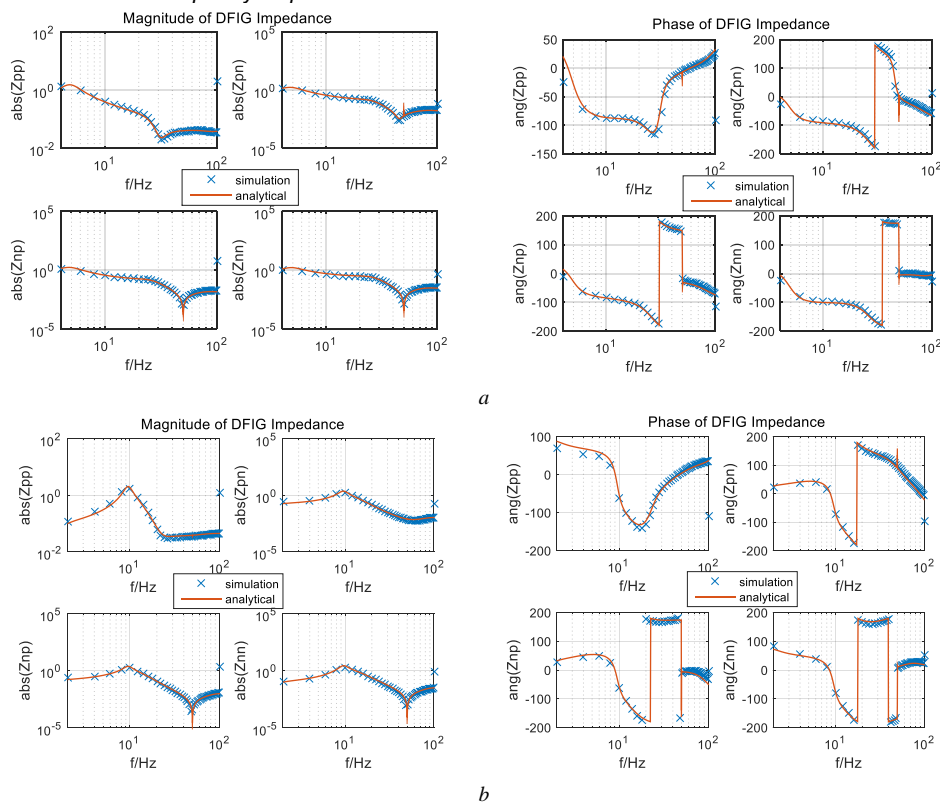
To calculate the impedance matrix, two sets of data are required, e.g. for the dq impedance, it can be calculated as:

$$\mathbf{Z}_{dq} = \begin{bmatrix} U_{d1} & U_{d2} \\ U_{q1} & U_{q2} \end{bmatrix} \begin{bmatrix} I_{d1} & I_{d2} \\ I_{q1} & I_{q2} \end{bmatrix}^{-1} \quad (11)$$

Hence, two sets of independent perturbations at each frequency are required to obtain the independent columns e.g. $\begin{bmatrix} I_{d1} & I_{q1} \end{bmatrix}^T$ and $\begin{bmatrix} I_{d2} & I_{q2} \end{bmatrix}^T$. This is fulfilled by injecting the positive and negative sequence perturbations in this case.

Afterward, simulation data are sent to MATLAB for frequency-domain analysis and impedance calculation. A flowchart of this process is briefly shown in Fig. 3.

3.2. Comparison of the detailed DFIG model with the measured frequency responses

Fig. 4 presents the Bode plots of the detailed DFIG model in comparison with the measured frequency responses. Both sub- and super-synchronous conditions are taken into account (the sub-synchronous mode denotes the generator speed is less than the grid frequency, whereas the super-synchronous mode is the opposite). Main circuit and control parameters are given in appendix 8.3.

From these figures it can be obtained that, in general, the analytical impedance plots are well-matched with the simulations both in magnitude and phase, indicating the detailed DFIG model i.e. (10) is effective. This also implies that the proposed model can accurately capture the dynamics within the frequency range of interest, and is effective for frequency-domain analysis.

Please note that (10) is in admittance format, it is inversed to get the corresponding DFIG impedance.

a

b

Fig. 4 *Comparison of the detailed DFIG model with simulation (current controller bandwidth for both GSC and RSC are 200 Hz, PLL bandwidth is 20 Hz, PQ and dc voltage controller bandwidth are 20 Hz. Grid SCR is 4.)*

(a) Bode plots at sub-synchronous operation ($\boldsymbol{\omega_{r0}}$= 0.8 p.u., magnitude units are ohm in dB format, phase units are in degree)
(b) Bode plots at super-synchronous operation ($\boldsymbol{\omega_{r0}}$= 1.2 p.u., magnitude units are ohm in dB format, phase units are in degree)

Further, it can be identified that the impedance shapes are very different when the operating modes are changed (e.g. by comparing the impedance characteristics under super- and sub-synchronous mode). This implies that the power flow may have some impacts on DFIG stability, particularly the power flow direction since the converter power flow is inverted if the DFIG changes from super- to sub-synchronous mode. More discussion on this will be provided in section 4 along with the model reductions.

Back to the analysis of the impedance characteristics, it can be seen that the Z_{pp} under sub-synchronous mode (Fig. 4 (a)) exhibits more capacitive characteristics than the super-synchronous mode (Fig. 4 (b)) at the low-frequency range. This implies the DFIG is more likely to be unstable under sub-synchronous mode when it is connected to a weak AC

4

grid. This mechanism is similar to the equivalent RLC circuit of a grid-tied VSC system [3] as introduced before. This finding also addresses the potential impacts of the power flow direction of the back-to-back converter on stability (i.e. super and sub-synchronous operating mode).

In addition, it can also be observed that the off-diagonal terms e.g. Z_{pn} and Z_{np} are not small compared to the diagonal terms e.g. Z_{pp} and Z_{nn}. Consequently, neglecting them may lead to inaccuracies on stability results as will be discussed in section 4.

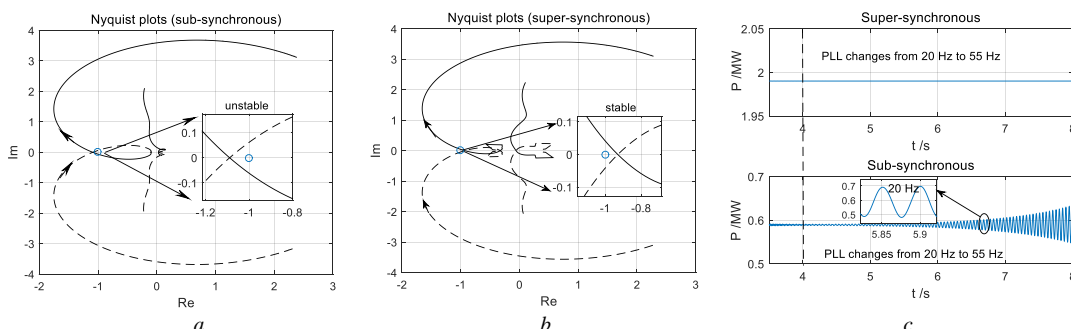### 3.3. Nyquist-based stability analysis under a weak AC grid condition

Since the DFIG and the AC grid forms a closed-loop system, the Nyquist criterion can be applied to study this closed-loop system stability by plotting its eigen-loci of the minor loop gain [13] in a complex plane. In this case, the minor loop gain is the multiplication of the DFIG admittance and the ac grid impedance. However, since the impedances under discussion are generally two-by-two matrices, the generalized Nyquist Criterion [15] has to be applied rather than the classic one. Therefore, the stability can be analyzed by plotting the eigenvalue loci of the loop gain $L(s) = \mathbf{Z}_{pn}^{S} \cdot \mathbf{Y}_{pn}^{DFIG}$ in a complex plane and counting their encirclements of the critical point (-1, 0 j).

Fig. 5 *Nyquist plots and time domain simulations (conditions are similar to the analysis in Fig. 4, except the PLL bandwidth)*

(a) Nyquist plots ($\omega_{r0} = 0.8$ p.u., PLL 55 Hz); *(b)* Nyquist plots ($\omega_{r0} = 1.2$ p.u., PLL 55 Hz) *(c)* Time domain verification of the Nyquist-based stability analysis, PLL bandwidth is increased from 20 Hz to 55 Hz at 4 s.

Typically, the DFIG is designed to be stable when connecting to an ideal ac grid. Hence, there are no right-hand poles in $\mathbf{Y}_{pn}^{DFIG}$, a similar consideration also applies to the grid $\mathbf{Z}_{pn}^{S}$. Consequently, any clockwise encirclements of the critical point (-1, 0 j) will result in an unstable system (one may refer [13] and [25] for more details).

The Nyquist plots of the DFIG system with a weak AC grid are shown in Fig. 5 (a) and (b). It can be identified that, under the sub-synchronous mode, the DFIG is unstable since one of the eigen-loci encircles the critical point in a clockwise direction. On the other hand, the DFIG is shown to be stable under super-synchronous mode. This observation regarding the impact of power flow direction justifies the previous finding in section 3.2, where the stability was qualitatively predicted according to the DFIG impedance characteristics.

A time domain simulation is further conducted to verify the Nyquist-based analysis. As shown in Fig. 5 (c), initially, the PLL bandwidth is set to 20 Hz to achieve a stable operation under both the sub- and super- synchronous modes. Then, it is increased to 55 Hz at 4s. It can be seen that, under the super-synchronous mode, the DFIG system is stable, which is consistent with the analysis of Fig. 5 (b). Whereas, under the sub-synchronous condition, the DFIG is unstable and exhibits a 20 Hz oscillation in dc voltage. Moreover, this simulation also implies is a marginally unstable case, because it takes a relatively long time for the oscillation to be observable since the PLL bandwidth change. This finding is consistent with the Nyquist plots in Fig. 5 (a), where the encirclement occurs close to the critical point.

In summary, the detailed DFIG model is effective for stability analysis, and it will be used as the reference model for the later comparative analysis.

4. Discussion on the reduced-order DFIG models for stability analysis

4.1. Derivation of the reduced-order models

Benefits from the modular modeling method, the reduced-order models can be assembled efficiently by setting some of the components to zero or removing some of the ports according to the model assumptions. In this section, four types of reduced-order models are considered:

Model.1: The off-diagonal terms of the detailed DFIG model in (10) are removed, i.e. $\mathbf{Y}_{pn}^{ml\_1} = diag\left(\mathbf{Y}_{pn}^{DFIG}\right)$. Thus the derived DFIG impedance model is decoupled.

Model.2: Only the RSC is considered, whereas the GSC is removed. Meanwhile, the dc voltage is assumed constant. The model can be derived from (6) by removing the dc port, i.e. $\mathbf{Y}_{pn}^{ml\_2} = -\mathbf{Y}_{pn}^{rsc}$.

Model.3: Only GSC is considered, the RSC is removed and replaced by a constant current source/load at the dc side. This model can be derived from (3) and (4) as:

$$\mathbf{Y}_{pn}^{ml\_3} = -\mathbf{Y}_{pn}^{gsc} + \mathbf{a}_{2\times1} \cdot \mathbf{b}_{1\times2} / \left(s \cdot C_{cap} + Y_{dc}^{gsc}\right).$$

Model.4: Model.2 and Model.3 are parallel-connected at the ac side, i.e. $\mathbf{Y}_{pn}^{ml\_4} = \mathbf{Y}_{pn}^{ml\_2} + \mathbf{Y}_{pn}^{ml\_3}$. This model is equivalent to assume that the RSC and the GSC are decoupled at the dc side. Note that the dc voltage control loop still exists in the GSC model.

5

To help illustration, a circuit description of these reduced-order models are drawn in Fig. 6.
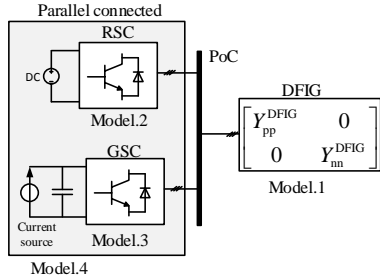

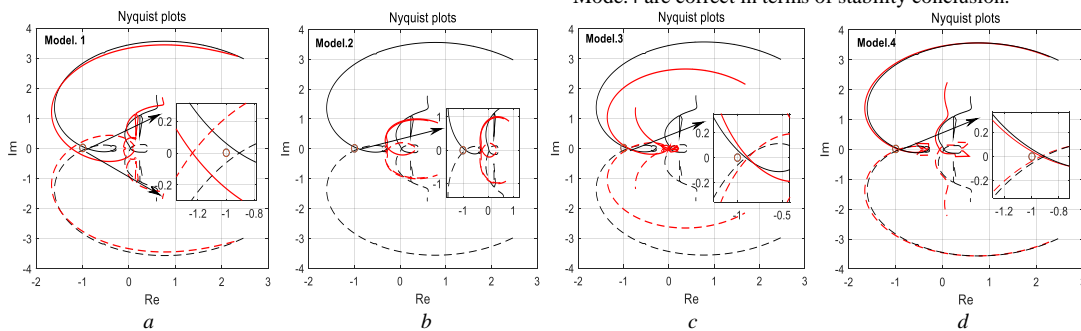**Fig. 6** *A circuit description of the reduced-order models*

Fig. 7 *Nyquist plots comparison of the reduced-order models (ω_{r0}=1.2 p.u., PLL bandwidth is 50 Hz, PQ and dc voltage controller bandwidth is 20 Hz, current controller bandwidth of GSC and RSC is 200 Hz, SCR is 4.)*

(a) Model.1; *(b)* Model.2; *(c)* Model.3; *(d)* Model.4 (black lines: the detailed model; red lines: the reduced models).

4.2. Evaluation of the reduced-order models on stability assessments

In the following, these reduced-order DFIG models will be compared with the detailed DFIG model in terms of Nyquist plots, so that the model assumptions on the accuracy of stability assessment can be intuitively revealed.

The Nyquist plots of the reduced-order models, as well as the detailed DFIG model, are shown in Fig.7 (a)-(d), where the super-synchronous operating mode is initially taken into account. As indicated by the detailed DFIG model (black lines), in this case, the DFIG is stable and this conclusion will be the reference for the reduced-order models.

By comparing the Nyquist plots of the reduced-order models with the detailed DFIG model, it can be obtained that Model.1 and Model.2 are wrong, whereas Model.3 and Mode.4 are correct in terms of stability conclusion.

Specifically, although Model.1 and Model.2 draw a wrong stability conclusion in this case, the Model.1 performs much better than the Model.2 according to their eigenvalue loci.

In the case of Model.1, its eigen-loci are very close to the detailed model at the high-frequency range, whereas exhibiting some inaccuracies at low-frequency range, this leads to an over-pessimistic stability conclusion as depicted in Fig.7 (a).

On the other hand, the eigen-loci of Model.2 are extremely different from the detailed DFIG model, which are far away from the critical point. This implies that the RSC is less risky in instability. This makes sense because the large magnetizing inductance of DFIG can overtake the control effects of the RSC, resulting in an inductive impedance characteristic. It is intuitive to know that an inductive DFIG impedance when connecting to an inductive grid will be very stable. Since this large discrepancy in the eigen-loci, the Model.2 cannot be used for stability analysis.

Further, according to Fig.7 (c) it can be obtained that the eigen-loci of the Model.3 are improved in comparison with the Model.2. This also implies that the GSC is more important in determining the DFIG stability than the RSC. In this case, the Model.3 can predict the same stability conclusion as the detailed DFIG model, though there are some evident differences in the shape of the eigen-loci.

This discrepancy in eigen-loci can be reduced by further paralleling the Model.3 with the Model.2, i.e. the Model.4. According to the Fig.7 (d), the Model.4 is shown to

be a good approximation to the detailed DFIG model. Moreover, the modelling work for Model.4 is much less than the detailed one due to the fact that the dc-side is assumed to be decoupled, which means the GSC and RSC can be modelled separately.

Since the Model.3 and Model.4 draw the correct stability conclusion in this case, meanwhile, as addressed before the effects of power flow direction should not be overlooked, hence these two reduced-order models will be tested under sub-synchronous mode further, and the results are shown in Fig. 8.

From Fig. 8 (a) it can be obtained that, the Model.3 predicts wrong stability conclusion in this case, mainly due to the change of the power flow direction. In combination with the analysis under the super-synchronous mode, it can be concluded that the Model.3 is slightly optimistic for DFIG stability analysis. On the other hand, the Model.4 still performs well under this condition, exhibiting good accuracy both in eigen-loci and stability conclusion, as illustrated in Fig. 8 (b).

To verify the above analysis, a time domain simulation is conducted in PSCAD/EMTDC, from which the dc voltage responses of the detailed DFIG model, Model.3 and Model.4 are compared in Fig. 8 (c). It can be observed that after the PLL bandwidth changes from 20 Hz to 55 Hz (i.e. the value of Nyquist plots) at 3s, both the detailed DFIG model and the Model.4 start oscillating after a relatively long time, indicating a marginally unstable condition. However, the Model.3 is shown to be stable since the dc voltage remains

6

ReView by River Valley Technologies

IET Power Electronics

This article has been accepted for publication in a future issue of this journal, but has not been fully edited.
Content may change prior to final publication in an issue of the journal. To cite the paper please use the doi provided on the Digital Library page.

steady. This simulation shows that the former remarks on the Model.3 and Model.4 are correct.

One may also observe that the dc voltage response from the Model.4 increases faster than the detailed model.

This finding can also be justified from the Nyquist plots in Fig. 8 (b), where the eigen-loci of Model.4 are located slightly to the left side of the detailed DFIG model, implying more negative damping in time domain responses.
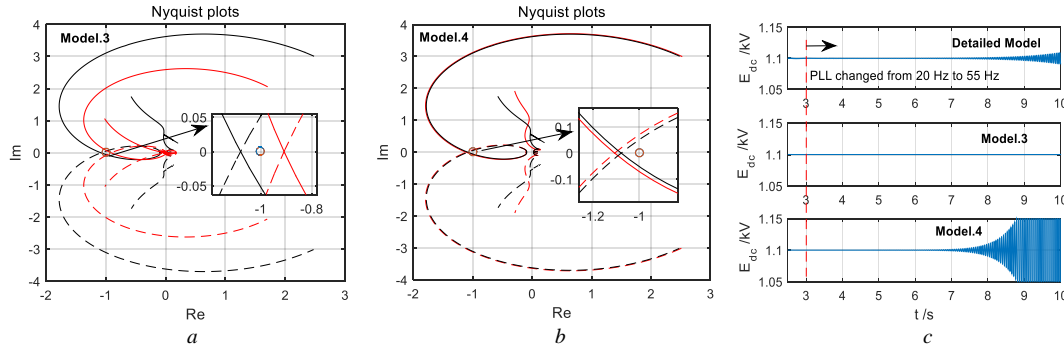

Fig. 8 *Nyquist plots comparison and simulation ($\omega r0=0.8$ p.u., PLL bandwidth is 55 Hz, other conditions are the same as Fig.7, red lines denotes reduced models, black lines denote detailed model.)*

(a) Nyquist plots of the Model.1; *(b)* Nyquist plots of the Model.2; *(c)* Time domain simulations; (black lines: the detailed model; red lines: the reduced models).

Besides, it is worth to explain that time domain simulations of Model.1 and Model.2 are not shown because Model.1 has no physical meaning since it is mathematically deduced from the detailed DFIG model, whereas Model.2 is obviously not suitable for stability analysis as concluded before. In fact, Model.2 has been tested in simulation, and the results are consistent with the Nyquist plots, in which the Model.2 can remain stable even under an extreme worse condition (e.g. a very fast PLL, e.g. 100 Hz and an extremely weak ac grid, e.g. SCR = 2). This is the consequence of the large discrepancy in eigen-loci as addressed before.

5. Conclusion

This work derives a detailed DFIG impedance model, along with four types of reduced-order models through the modular modeling approach. The detailed DFIG model is verified by measured frequency responses as well as its correctness on stability analysis. Several significant concerns on the reduced-order models are clarified as follows:
1) The Model.1, obtained with omitting the off-diagonal terms of the detailed DFIG impedance model is shown to be over-pessimistic for stability analysis.
2) The Model.2, only with a detailed modelling of the RSC cannot be used for stability analysis due to its large discrepancy in eigen-loci compared with the detailed DFIG model.
3) The Model.3, only with a detailed modelling of the GSC is slightly optimistic in terms of the stability conclusion, though some evident differences in eigen-loci are observed when compared with the detailed DFIG model.
4) The Model.4, obtained by paralleling the Model. 2 with the Model. 3 provides the best approximation to the detailed DFIG model. Thus, it can be a good candidate and is more efficient for stability analysis since less modelling work is required compared to the detailed one.

It is worth to note again that these conclusions regarding the DFIG model reductions are drawn under a non-compensated ac grid.

7. References

[1] Teodorescu, R., Liserre, M., Rodriguez, P., "Introduction," in Grid converters for photovoltaic and wind power systems, Chichester, United Kingdom: John Wiley & Sons, pp. 1–4, 2011.

[2] Sorensen, P., Cutululis, N.A., Rodríguez, A.V. *et al*: "Power fluctuations from large wind farms" IEEE Trans. Power Syst., 2007, 22(3), pp. 958-965.

[3] Zhang, C., Cai, X., Li, Z. *et al*: "Properties and Physical Interpretation of the Dynamic Interactions between Voltage Source Converters and Grid: Electrical Oscillation and Its Stability Control" IET Power Electron, 2017, 10 (8), pp. 894–902.

[4] Bongiorno, M., Petersson, A., Agneholm, E.: "The impact of wind farms on subsynchronous resonance in power systems" Elforsk, stochholm, April 2011.

[5] Choo, Y. C., Agalgaonkar, A. P., Muttaqi K. M., *et al*: "Subsynchronous torsional interaction behaviour of wind turbine-generator unit connected to an HVDC system" IECON on IEEE Industrial Electronics Society, Glendale, 2010, pp. 996-1002.

[6] Fan, L., Kavasseri, R., Miao,Z. L. *et al*: "Modeling of DFIG-Based Wind Farms for SSR Analysis" IEEE Trans. Power Del, 2010, 25(4), pp. 2073-2082.

[7] Fan, L., Zhu, C., Miao, Z., *et al*:"Modal Analysis of a DFIG-Based Wind Farm Interfaced With a Series Compensated Network" IEEE Trans. Energy Convers, 2011, 26(4), pp. 1010-1020.

[8] Zhu, C., Fan, L., Hu, M.: "Control and analysis of DFIG-based wind turbines in a series compensated network for

7

ReView by River Valley Technologies

This article has been accepted for publication in a future issue of this journal, but has not been fully edited.
Content may change prior to final publication in an issue of the journal. To cite the paper please use the doi provided on the Digital Library page.

IET Power Electronics

SSR damping" IEEE PES General Meeting, Minneapolis, MN, 2010, pp. 1-6.

[9] El-Moursi, M. S., Jensen, B. B., Abdel-Rahman, M. H.: "Novel STATCOM Controller for Mitigating SSR and Damping Power System Oscillations in a Series Compensated Wind Park" IEEE Trans. Power Electron, 2010, 25 (2), pp. 429-441.

[10] Liu, H., Xie, X.R., He, J., *et al*:"Subsynchronous interaction between direct-drive PMSG based wind farms and weak AC networks" IEEE Trans. Power Syst, 2017, 32(6), 4708-4720.

[11] Fan, L. and Miao, Z.:"An Explanation of Oscillations Due to Wind Power Plants Weak Grid Interconnection" IEEE Trans. Sustainable Enery, 2018, 9 (1), pp. 488-490.

[12] Sun, J.: "Small-Signal Methods for AC Distributed Power Systems–A Review," in IEEE ESTS., Baltimore, Maryland, 2009, pp .44–52.

[13] Sun, J.: "Impedance-based stability criterion for grid-connected inverters" IEEE Trans. Power Electron, 2011, 26 (11), pp. 3075-3078.

[14] Cespedes, M., Sun, J.: "Impedance Modeling and Analysis of Grid-Connected Voltage-Source Converters" IEEE Trans. Power Electron, 2014, 29 (3), pp. 1254–1261.

[15] Wen, B., Boroyevich, D., Burgos, R. *et al*: "Small-Signal Stability Analysis of Three-Phase AC Systems in the Presence of Constant Power Loads Based on Measured d-q Frame Impedances" IEEE Trans. Power Electron, 2015, 30(10), pp.5952–5963.

[16] Shah, S., Parsa, L.: "Impedance modeling of three-phase voltage source converters in dq, sequence, and phasor domains," IEEE Trans Energy Convers, 32(3), 1139-1150.

[17] Rygg, A., Molinas, M., Zhang, C. *et al*: "A modified sequence domain impedance definition and its equivalence to the dq-domain impedance definition for the stability analysis of ac power electronic systems," IEEE J. Sel. Topics. Power Electron, 2016, 4(4), pp.1382–1396.

[18] Harnefors, L.: "Modeling of three-phase dynamic systems using complex transfer functions and transfer matrices" IEEE Trans. Industrial Electron, 2007, 54(4), 2239-2248.

[19] Wang, X.F., Harnefors, L., Blaabjerg, F. *et al*: "A Unified Impedance Model of Voltage-Source Converters with Phase-Locked Loop Effect," IEEE ECCE, United States, 2016, pp. 1–8.

[20] Bakhshizadeh, M. K., Wang, X.F., Blaabjerg, F., *et al*: "Couplings in Phase Domain Impedance Modeling of Grid-Connected Converters," IEEE Trans. Power Electron, 2016, 31(10), pp. 6792–6796.

[21] Xu, Y., Nian, H., Wang, T., Chen, L. *et al*, "Frequency coupling characteristic modeling and stability analysis of doubly fed induction generator," IEEE Trans. Energy Convers, 2018 (online).

[22] Vieto, I., Sun, J.: "Sequence impedance modeling and analysis of type-III wind turbines," IEEE Trans. Energy Convers, 2017. (on line).

[23] Wu, B., Lang, Y., Zargari, N. *et al*: "Chapter 7" in Power conversion and control of wind energy systems, Chichester, United Kingdom: John Wiley & Sons, 2011.

[24] Zhang, C., Cai, X., Rygg, A. *et al*: "Sequence domain siso equivalent models of a grid-tied voltage source converter system for small-signal stability analysis," IEEE Trans Energy Convers, 2017, 33(2), pp.741-749.

[25] Wen, B., Boroyevich, D., Burgos, R., *et al*, "Inverse Nyquist Stability Criterion for Grid-Tied Inverters," in IEEE Transactions on Power Electronics, 2017, 32(2), pp. 1548-1556.

8. Appendices

8.1. Transfer functions of the GSC module in the modified sequence domain

Derivation of (1): The *dq* variables can be written in a more compact vector format as: $i_{dq} = i_d + ji_q$. Then the current vector in PLL frame can be derived as:

$$\boldsymbol{i}_{pll}^{gsc} + \boldsymbol{I}_{c0} = \left(\boldsymbol{i}_{dq}^{gsc} + \boldsymbol{I}_{c0}\right)e^{-j\Delta\theta_{pll}} \approx \left(\boldsymbol{i}_{dq}^{gsc} + \boldsymbol{I}_{c0}\right)\left(1 - j\Delta\theta_{pll}\right) \quad (A.1)$$

hence,

$$\boldsymbol{i}_{pll}^{gsc} = \boldsymbol{i}_{dq}^{gsc} - \boldsymbol{I}_{c0}j\Delta\theta_{pll} \quad (A.2)$$

$\boldsymbol{i}_{pll}^{gsc}$ is the feedback current vector for controls.

The outputs of the current controller are duty cycles. Similarly, they can be written as:

$$\boldsymbol{d}_{pll}^{gsc} + \boldsymbol{D}_{c0} = \left(\boldsymbol{d}_{dq}^{gsc} + \boldsymbol{D}_{c0}\right)e^{-j\Delta\theta_{pll}} \approx \left(\boldsymbol{d}_{dq}^{gsc} + \boldsymbol{D}_{c0}\right)\left(1 - j\Delta\theta_{pll}\right) \quad (A.3)$$

then,

$$\boldsymbol{d}_{pll}^{gsc} = \boldsymbol{d}_{dq}^{gsc} - j\boldsymbol{D}_{c0}\Delta\theta_{pll} \quad (A.4)$$

is obtained.

For the PLL, its small signal input is the projection of the PoC voltage on the q axis, which is $u_{pllq} = u_q - U_0\Delta\theta_{pll}$.

Substituting it into the PLL forward gain yields: $\Delta\theta_{pll} = \frac{H_{pll}(s)}{s} \cdot u_{pllq}$. Hence, the PLL transfer function is:

$$\Delta\theta_{pll} = \frac{U_0 H_{pll}(s)}{1 + U_0 H_{pll}(s)}\frac{u_q}{U_0} = T_{pll}(s)\frac{u_q}{U_0} \quad (A.5)$$

The output voltage vector of the GSC is:

$$\boldsymbol{u}_{dq}^{gsc} + \boldsymbol{U}_{c0} = \left(\boldsymbol{d}_{dq}^{gsc} + \boldsymbol{D}_{c0}\right)\left(u_{dc} + V_{dc0}\right) \quad (A.6)$$

hence, its linearized model is obtained as:

$$\boldsymbol{u}_{dq}^{gsc} = \boldsymbol{D}_{c0}u_{dc} + V_{dc0}\boldsymbol{d}_{dq}^{gsc} \quad (A.7)$$

The relationship between the ac and the dc side currents can be established according to the power balance as:

$$i_{dc}^{gsc} = 1.5\,\text{Re}\left\{\boldsymbol{D}_{c0}\left(\boldsymbol{i}_{dq}^{gsc}\right)^* + \boldsymbol{I}_{c0}^*\boldsymbol{d}_{dq}^{gsc}\right\} \quad (A.8)$$

Assembling (A.2), (A.4), (A.5), (A.7) via the control diagram in Fig. 1 can derive (1).

Transfer-function blocks: Afterwards, transforming (1) into the modified sequence domain through (2), then the GSC module (with three ports) is obtained, and its associated transfer-functions are given as follows:

$$\boldsymbol{Y}_{pn}^{gsc} = -diag_{2\times2}\left(\frac{1}{H_c V_{dc0} + Z_p^f}, \frac{1}{H_c V_{dc0} + Z_n^f}\right)\begin{bmatrix} 1 - G_p^{pll0} & G_p^{pll0} \\ G_n^{pll0} & 1 - G_n^{pll0} \end{bmatrix};$$

8

$$a_{2\times1} = 0.5\begin{bmatrix} \dfrac{H_c H_{dc} V_{dc0} + D_{c0}}{H_c V_{dc0} + Z_p^f} & \dfrac{H_c H_{dc} V_{dc0} + D_{c0}^*}{H_c V_{dc0} + Z_n^f} \end{bmatrix}^T ;$$

$$b_{1\times2} = \frac{3}{2}\left\{ \begin{bmatrix} D_{c0}^* + \dfrac{I_{c0}^* Z_p^f}{V_{dc0}} & D_{c0} + \dfrac{I_{c0} Z_n^f}{V_{dc0}} \end{bmatrix} Y_{pn}^{gsc} + \begin{bmatrix} I_{c0}^* & I_{c0} \end{bmatrix}\dfrac{1}{V_{dc0}} \right\};$$

$$Y_{dc}^{gsc} = \frac{3}{2}\begin{bmatrix} D_{c0}^* + \dfrac{I_{c0}^* Z_p^f}{V_{dc0}} & D_{c0}^* + \dfrac{I_{c0} Z_n^f}{V_{dc0}} \end{bmatrix}a_{2\times1} - \dfrac{P_{c0}}{V_{dc0}^2}.$$

where, $Z_p^f(s) = sL_f + j\omega_s L_f$, $G_n^{pll0}(s) = \left(G_p^{pll0}(s)\right)^*$ and

$Z_n^f(s) = \left(Z_p^f(s)\right)^*$. $G_p^{pll0}(s) = V_{dc0}\left(H_c I_{c0} + D_{c0}\right)\dfrac{T_{pll}(s)}{2U_0}$. Note

that the conjugation operator only applied to the coefficients of complex-value functions, e.g. $Z_n^f(s) = sL_f - j\omega_s L_f$.

8.2. Transfer functions of the RSC module in the modified sequence domain

Derivation of (5): The *dq* domain model of the RSC and the generator winding dynamics can be established similarly as the GSC. In which, the current vector feedback is:

$$i_{pll}^r = i_{dq}^r - jI_{r0}\Delta\theta_{pll} \tag{A.9}$$

The current controller output is:

$$d_{pll}^r = d_{dq}^r - jD_{r0}\Delta\theta_{pll} \tag{A.10}$$

The RSC output voltage is:

$$u_{dq}^r = D_{r0}u_{dc}^{rsc} + V_{dc0}d_{dq}^r \tag{A.11}$$

The generator winding dynamics can be obtained from its flux-linkage and voltage equations:

$$u_{dq}^r = R_r i_{dq}^r + \left(s + js_0\omega_s\right)\left(L_r i_{dq}^r - L_m i_{dq}^{rsc}\right) \tag{A.12}$$

is the rotor voltage equation.

$$u_{dq}^{poc} = -R_s i_{dq}^{rsc} + \left(s + js_0\omega_s\right)\left(L_m i_{dq}^r - L_s i_{dq}^{rsc}\right) \tag{A.13}$$

is the stator voltage equation.

Assembling (A.9)-(A.13) via the control diagram in Fig. 1 can derive (5).

Transfer-function blocks: Afterwards, transforming (5) into the modified sequence domain through (2), then the RSC module (with three ports) is obtained, and the associated transfer-functions are given as follows:

$$Y_{pn}^{rsc} = diag_{2\times2}\left(Y_p^{IOP}, Y_n^{IOP}\right)\cdot$$
$$\begin{bmatrix} k_p^m - G_p^{pll0}V_{dc0} & 1.5H_c H_s I_{s0}V_{dc0} + G_p^{pll0}V_{dc0} \\ 1.5H_c H_s I_{s0}V_{dc0} + G_n^{pll0}V_{dc0} & k_n^m - G_n^{pll0}V_{dc0} \end{bmatrix};$$

$$c_{2\times1} = \frac{1}{2}\begin{bmatrix} D_{r0}Y_p^{IOP} \\ D_{r0}^*Y_n^{IOP} \end{bmatrix};$$

$$d_{1\times2} = \frac{3}{2V_{dc0}}\left\{ \begin{bmatrix} V_{dc0}D_{r0}^* + I_{r0}^*Z_p^{lr} & V_{dc0}D_{r0} + I_{r0}Z_n^{lr} \end{bmatrix}Y_{pn}^{rsc} \\ + \begin{bmatrix} \dfrac{V_{dc0}D_{r0}^*}{Z_p^m} + I_{r0}^*k_p^m & \dfrac{V_{dc0}D_{r0}}{Z_n^m} + I_{r0}k_n^m \end{bmatrix} \right\};$$

$$Y_{dc}^{rsc} = \frac{3}{2V_{dc0}}\begin{bmatrix} V_{dc0}D_{r0}^* + I_{r0}^*Z_p^{lr} & V_{dc0}D_{r0} + I_{r0}Z_n^{lr} \end{bmatrix}c_{2\times1} - \dfrac{P_{r0}}{V_{dc0}^2}.$$

where, $Y_p^{IOP} = \dfrac{1}{H_c V_{dc0}\left(1.5U_{s0}^* H_s + 1\right) + Z_p^{Lr}}$, $Y_n^{IOP} = \left(Y_p^{IOP}\right)^*$,

$Z_p^{lr} = sL_{lr} + R_r + js_0\omega_s L_{lr}$, $Z_n^{lr} = \left(Z_p^{lr}\right)^*$ $Z_p^{Lr} = sL_r + R_r + js_0\omega_s L_r$,

$Z_n^{Lr} = \left(Z_p^{Lr}\right)^*$, $Z_p^{Lm} = sL_m + j\omega_s L_m$, $Z_n^{Lm} = \left(Z_p^{Lm}\right)^*$, $k_p^m = \dfrac{Z_p^r}{Z_p^m}$,

$k_n^m = \left(k_p^m\right)^*$.

8.3. DFIG and VSC parameters

Table 1 DFIG parameters

Name	value
Rating	2 MW
Voltage (mag per phase) U_0	563 V
Pole pairs	2
Turns ratio	1/3

Table 2 VSC parameters

Name	value
Rating	750 kW
Voltage (mag per phase) U_0	563 V
DC voltage V_{dc0}	1.1 kV
Filter inductance Lf	0.1 pu
DC capacitor C_{cap}	10 mF

9